A non-ordinary state-based Godunov-peridynamics formulation for strong shocks in solids
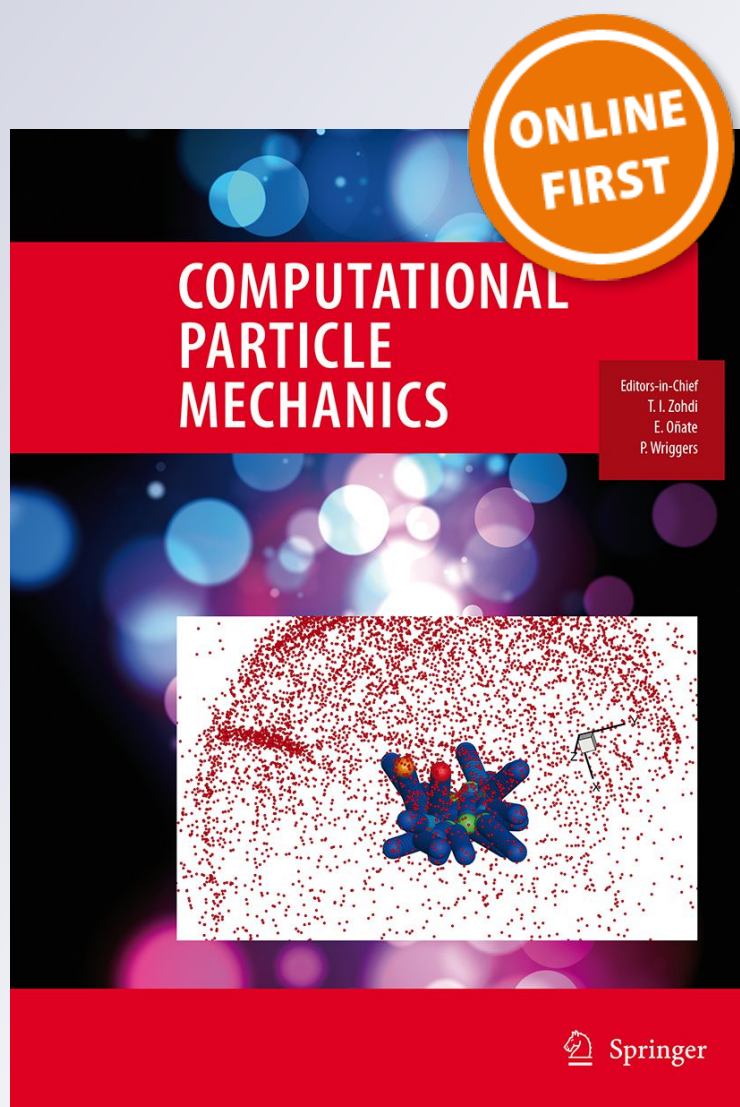
Guohua Zhou & Michael Hillman

COMPUTATIONAL PARTICLE MECHANICS

Editors-in-Chief
T. I. Zohdi
E. Oñate
P. Wriggers

ONLINE FIRST

🕮 Springer

🕮 Springer

Springer

A non-ordinary state-based Godunov-peridynamics formulation for strong shocks in solids

Guohua Zhou[1] · Michael Hillman[2]

Abstract

The theory and meshfree implementation of peridynamics has been proposed to model problems involving transient strong discontinuities such as dynamic fracture and fragment-impact problems. For effective application of numerical methods to these events, essential shock physics and Gibbs instability should be addressed. The Godunov scheme for shock treatment has been shown to be an effective approach for tackling these two issues but has not been considered yet for peridynamics. This work introduces a physics-based shock modeling formulation for non-ordinary state-based peridynamics, in which the Godunov scheme is introduced by embedding the Riemann solution into the force state, resulting in a shock formulation free of tuneable parameters. Several benchmark problems are solved to demonstrate the effectiveness of the proposed formulation for modeling problems involving shocks in solids.

Keywords Peridynamics · Meshfree · Shockwaves · Godunov scheme

1 Introduction

The theory of peridynamics [1,2] has been proposed to effectively model problems that involve dynamic strong discontinuities such as dynamic fracture and fragment-impact problems. It bypasses essential difficulties of classic continuum mechanics in fracture modeling due to the invalidity of taking spatial derivatives across cracks and necessity for geometric descriptions of arbitrary three-dimensional propagating crack surfaces, by directly working on integral forms of governing equations that do not involve spatial derivatives.

The first peridynamics model is called bond-based peridynamics [1] which was proposed to model the formation of discontinuities in elastic brittle solids. As a non-local theory, bonds are defined between a point and all of its neighboring points within a zone called a horizon. The two points in a single bond interact via a spring-like force depending on only the stretch of the bond itself, and cracks can be naturally modeled by the breakage of the bonds. This method has been applied to dynamic crack branching in brittle glass [3,4], impact and

damage of layered glass [5], and damage in concrete [6], among other problems.

However, the bond-based peridynamics formulation suffers from restrictions on the material response, for example, Poisson's ratio is limited to a fixed value. Meanwhile, constitutive laws need to be developed specifically for peridynamics. To overcome these limitations, state-based peridynamics [2] was introduced. In this formulation, the bond force depends on the collective deformation of all the bonds within a horizon rather than a single bond independently, as in the bond-based model. The so-called non-ordinary state-based peridynamics based on correspondence [2] defines the constitutive response through a non-local deformation gradient and can thus incorporate classical constitutive models. This approach has been applied to ballistic impact of aluminum panels [7], high-velocity impact [8], and dynamic fracture of aluminum [9].

Although the non-ordinary state-based peridynamics has been widely applied to model high strain rate problems, there is limited work published on shock modeling. Shock wave propagation is an important physics to be considered in numerical methods for problems such as high-velocity impact and blast, where peridynamics has great advantages due to its natural ability to model transient discontinuities. In [10,11], the artificial viscosity technique was employed to treat shocks in peridynamics. This approach is simple

✉ Michael Hillman
mhillman@psu.edu

[1] Optimal Inc., Plymouth, MI 48170, USA

[2] The Pennsylvania State University, University Park, PA 16802, USA

to implement, but involves tunable parameters, which is undesirable since it leads to parameter-dependent results, which are not objective. In [12], artificial dissipation via a rate-dependent material model was introduced for the same purpose, with similar limitations.

An effective approach for shock modeling is the class of Godunov schemes originating from the method proposed by Godunov [13] under the finite difference framework. In these methods, the jump conditions and the entropy solution are embedded by solving a Riemann problem defined at cell interfaces. They have been extended to the discontinuous Galerkin method [14], smoothed particle hydrodynamics [15], the finite point method [16], among other methods [17–22]. Higher-order Godunov schemes [23] have also been developed to enhance accuracy. Under the reproducing kernel particle method framework [24,25] with stabilized conforming nodal integration (SCNI) [26], a Riemann-SCNI method [27,28] has been developed to introduce the Godunov scheme by a Riemann solution enriched pressure gradient, smoothed over SCNI cells.

In this paper, the Godunov scheme is embedded into the non-ordinary state-based peridynamics, and the resulting formulation is termed Godunov-peridynamics. First, the force state is expressed in terms of Cauchy stress and separated into volumetric and deviatoric contributions since the pressure dominates the Cauchy stress under strong shocks. Effective surface information between two points is then obtained by drawing an analogy between the resulting discrete peridynamic formulation and the finite volume method. This surface information is then used to define a Riemann problem between two points, and the Riemann solution is then employed in the volumetric force state to embed shock physics into state-based peridynamics.

The remainder of this paper is organized as follows. In Sect. 2, the non-ordinary state-based peridynamics formulation is reviewed. In Sect. 3, the Godunov-peridynamics formulation is then introduced. Numerical implementation of the proposed method is given in Sect. 4. Numerical results are then presented in Sect. 5 to demonstrate the effectiveness of the proposed method, followed by discussions and conclusions in Sect. 6.

2 Non-ordinary state-based peridynamics formulation

In this section, we briefly review the non-ordinary state-based peridynamics formulation [2]. Let $\mathbf{x}$ and $\mathbf{X}$ denote coordinates in the deformed and undeformed configuration, respectively. A continuum point $\mathbf{X}$ interacts non-locally with its neighbors within a horizon H with measure δ as shown in Fig. 1. The bond of a point $\mathbf{X}_I$ with another point $\mathbf{X}_J$ in the undeformed configuration is

$$\mathbf{X}_{I:J} = \mathbf{X}_J - \mathbf{X}_I. \tag{1}$$

The same bond in the deformed configuration is denoted as

$$\mathbf{x}_{I:J} = \mathbf{x}_J - \mathbf{x}_I. \tag{2}$$

A non-local deformation gradient $\mathbf{F}_I$ at point I can be computed via the principle of constitutive correspondence [2] as

$$\mathbf{F}_I = \left(\int_{H_{\mathbf{X}_I}} \omega_{I:J} \mathbf{x}_{I:J} \otimes \mathbf{X}_{I:J} \mathrm{d}V_{\mathbf{X}_J} \right) \cdot \mathbf{K}_I^{-1}, \tag{3}$$

where $\mathbf{K}_I$ is the reference shape tensor defined as

$$\mathbf{K}_I = \int_{H_{\mathbf{X}_I}} \omega_{I:J} \mathbf{X}_{I:J} \otimes \mathbf{X}_{I:J} \mathrm{d}V_{\mathbf{X}_J}, \tag{4}$$

and $\omega_{I:J}$ is the so-called influence function which is a function of the distance between point I and J. In this paper, the Lagrangian peridynamics formulation is adopted; the influence function is defined in terms of material distance, and $H_{\mathbf{X}_I}$ and $\mathrm{d}V_{\mathbf{X}_J}$ in the above equations are the horizon of point I and volume associated with point J, respectively, in the undeformed configuration.

For the influence function, the following cubic spline function is chosen:

$$\omega_{I:J}\langle \mathbf{X}_{I:J} \rangle = \begin{cases} \frac{2}{3} - 4\left|\frac{\mathbf{X}_{I:J}}{\delta}\right|^2 + 4\left|\frac{\mathbf{X}_{I:J}}{\delta}\right|^3 & \text{for} \quad 0 \leq \left|\frac{\mathbf{X}_{I:J}}{\delta}\right| \leq \frac{1}{2}, \\ \frac{4}{3} - 4\left|\frac{\mathbf{X}_{I:J}}{\delta}\right| + 4\left|\frac{\mathbf{X}_{I:J}}{\delta}\right|^2 - \frac{4}{3}\left|\frac{\mathbf{X}_{I:J}}{\delta}\right| & \text{for} \quad \frac{1}{2} \leq \left|\frac{\mathbf{X}_{I:J}}{\delta}\right| \leq 1, \\ 0 & \text{otherwise,} \end{cases} \tag{5}$$

where δ is the radius of the horizon $H_{\mathbf{X}_I}$ as shown in Fig. 1a. The above influence function smoothly vanishes at the horizon boundary, which helps to improve the accuracy of numerical integration [29].

The force state between point I and J in terms of the first Piola–Kirchhoff stress tensor $\boldsymbol{\sigma}$ under correspondence is computed from the state $\underline{\mathbf{T}}_{I:J}$ acting on a bond $\mathbf{X}_{I:J}$:

$$\underline{\mathbf{T}}_{I:J}\langle \mathbf{X}_{I:J} \rangle = \omega_{I:J} \boldsymbol{\sigma}_I(\mathbf{F}_I) \cdot \mathbf{K}_I^{-1} \cdot \mathbf{X}_{I:J} \tag{6}$$

where $\boldsymbol{\sigma}_I(\mathbf{F}_I)$ is given by the constitutive model. The angle bracket in the above is used to denote the variable that a state operates on. The final equation of motion in the non-ordinary state-based peridynamics formulation at a point I is

$$\rho_I \ddot{\mathbf{u}}_I - \int_{H_{\mathbf{X}_I}} \left(\underline{\mathbf{T}}_{I:J}\langle \mathbf{X}_{I:J} \rangle - \underline{\mathbf{T}}_{J:I}\langle \mathbf{X}_{J:I} \rangle \right) \mathrm{d}V_{\mathbf{X}_J} - \mathbf{b}_I = 0, \tag{7}$$

where ρ_I is the density, $\ddot{\mathbf{u}}_I$ is the acceleration ($\mathbf{u}_I$ is the displacement), and $\mathbf{b}_I$ is the external body force density, at point I.
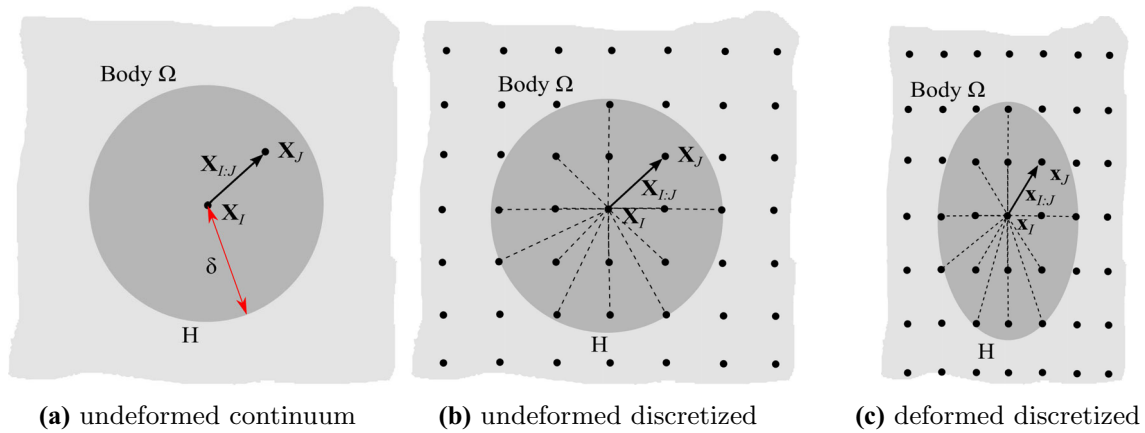
(a) undeformed continuum   **(b)** undeformed discretized   **(c)** deformed discretized

Fig. 1 Schematic of peridynamics representations: continuum and discrete cases

3 Godunov-peridynamics formulation

In the presence of shock waves, Eq. (7) with the force state given by (6) leads to severely oscillating nonphysical solutions due to lack of consideration of shock physics and Gibbs instability. To address these issues, the Godunov scheme [13] is introduced into the peridynamics formulation, which is discussed in this section.

3.1 Equation of motion

For convenience, the integrand of the second term in (7) is first expressed as

$$\hat{\underline{\mathbf{T}}}_{I:J} = \mathbf{T}_{I:J}\langle \mathbf{X}_{I:J}\rangle - \mathbf{T}_{J:I}\langle \mathbf{X}_{J:I}\rangle, \tag{8}$$

where $\hat{\underline{\mathbf{T}}}_{I:J}$ is the total force state between point I and J. Substitution of (6) into (8) yields the expression in terms of the first Piola–Kirchhoff stress

$$\hat{\underline{\mathbf{T}}}_{I:J} = \omega_{I:J}\boldsymbol{\sigma}_I(\mathbf{F}_I)\cdot\mathbf{K}_I^{-1}\cdot\mathbf{X}_{I:J} - \omega_{J:I}\boldsymbol{\sigma}_J(\mathbf{F}_J)\cdot\mathbf{K}_J^{-1}\cdot\mathbf{X}_{J:I}. \tag{9}$$

Making use of the fact that $\omega_{I:J} = \omega_{J:I}$ and $\mathbf{X}_{I:J} = -\mathbf{X}_{I:J}$, Eq. (9) can be rewritten as

$$\hat{\underline{\mathbf{T}}}_{I:J} = \omega_{I:J}\big(\boldsymbol{\sigma}_I(\mathbf{F}_I)\cdot\mathbf{K}_I^{-1} + \boldsymbol{\sigma}_J(\mathbf{F}_J)\cdot\mathbf{K}_J^{-1}\big)\cdot\mathbf{X}_{I:J}. \tag{10}$$

Employing the relationship between Cauchy stress $\boldsymbol{\tau}$ and the first Piola–Kirchhoff stress

$$\boldsymbol{\sigma} = \boldsymbol{\tau}\cdot\mathbf{F}^{-T}\det(\mathbf{F}) \tag{11}$$

where $\det(\mathbf{F})$ is the determinant of the non-local deformation gradient $\mathbf{F}$, Eq. (10) can be expressed as

$$\hat{\underline{\mathbf{T}}}_{I:J} = \omega_{I:J}\big(\boldsymbol{\tau}_I\cdot\mathbf{F}_I^{-T}\cdot\mathbf{K}_I^{-1}\det(\mathbf{F}_I)$$

$$+ \boldsymbol{\tau}_J\cdot\mathbf{F}_J^{-T}\cdot\mathbf{K}_J^{-1}\det(\mathbf{F}_J)\big)\cdot\mathbf{X}_{I:J}. \tag{12}$$

Since the pressure is the dominant portion of the Cauchy stress in strong shock problems, the stress tensor is split into volumetric $\boldsymbol{\tau}^{\text{v}}$ and deviatoric portions $\boldsymbol{\tau}^{\text{d}}$:

$$\boldsymbol{\tau}^{\text{v}} = P\mathbf{I}, \tag{13}$$

$$\boldsymbol{\tau}^{\text{d}} = \boldsymbol{\tau} - \boldsymbol{\tau}^{\text{v}}, \tag{14}$$

where $P = \frac{1}{3}(\tau_{11} + \tau_{22} + \tau_{33})$ is the pressure and $\mathbf{I}$ is the second-order identity tensor. Substituting (13) and (14) into (12) and collecting the deviatoric and volumetric portions yields

$$\hat{\underline{\mathbf{T}}}_{I:J} = \hat{\underline{\mathbf{T}}}_{I:J}^{\text{d}} + \hat{\underline{\mathbf{T}}}_{I:J}^{\text{v}}, \tag{15}$$

where

$$\hat{\underline{\mathbf{T}}}_{I:J}^{\text{d}} = \omega_{I:J}\big(\boldsymbol{\tau}_I^{\text{d}}\cdot\mathbf{F}_I^{-T}\cdot\mathbf{K}_I^{-1}\det(\mathbf{F}_I)$$

$$+ \boldsymbol{\tau}_J^{\text{d}}\cdot\mathbf{F}_J^{-T}\cdot\mathbf{K}_J^{-1}\det(\mathbf{F}_J)\big)\cdot\mathbf{X}_{I:J} \tag{16}$$

and

$$\hat{\underline{\mathbf{T}}}_{I:J}^{\text{v}} = \omega_{I:J}\big(P_I\mathbf{F}_I^{-T}\cdot\mathbf{K}_I^{-1}\det(\mathbf{F}_I)$$

$$+ P_J\mathbf{F}_J^{-T}\cdot\mathbf{K}_J^{-1}\det(\mathbf{F}_J)\big)\cdot\mathbf{X}_{I:J} \tag{17}$$

are the deviatoric and volumetric contributions, respectively. When applied to problems with strong shocks, the solution obtained by using these force states shows severe oscillations as the shock physics and Gibbs instability are not addressed. In this paper, the essential shock physics is introduced into the volumetric force state by embedding Godunov scheme, which is to be discussed next.

In Eq. (17), on the right-hand side, the first term involving P_I and the second term involving P_J physically represent the contribution to the volumetric force state between the two

points I and J from each pressure of the points, or in other words they represent the force exchange between points I and J due to pressure. In this paper, we introduce the Godunov scheme by solving the Riemann problem between point I and J to enrich this exchange. After solving the Riemann problem via a Riemann solver, the Riemann solution enriched pressure and velocity are obtained $\{P_{IJ}^*, \mathbf{v}_I^*, \}$ ('*' denotes the Riemann solution), and P_{IJ}^* is then used to replace the P_I and P_J in Eq. (17), and in this manner, the entropy solution and jump conditions are embedded into the force state. Accordingly, $\hat{\underline{\mathbf{T}}}_{I:J}^{\mathrm{v}}$ becomes $\hat{\underline{\mathbf{T}}}_{I:J}^{\mathrm{v*}}$ and (17) becomes

$$\hat{\underline{\mathbf{T}}}_{I:J}^{\mathrm{v*}} = \omega_{I:J} P_{IJ}^* \big(\det(\mathbf{F}_I)\mathbf{F}_I^{-1} \cdot \mathbf{K}_I^{-1} + \det(\mathbf{F}_J)\mathbf{F}_J^{-1} \cdot \mathbf{K}_J^{-1}\big) \cdot \mathbf{X}_{I:J},$$
(18)

where P_{IJ}^* is the pressure solution of the Riemann problem between point I and J. The details about how to define and solve the Riemann problem are discussed in Sects. 3.2 and 4.2.

Finally, the equation of motion after embedding the Godunov scheme is

$$\rho_I \ddot{\mathbf{u}}_I - \int_{\mathrm{H}_{\mathbf{x}_I}} \left[\hat{\underline{\mathbf{T}}}_{I:J}^{\mathrm{d}} \langle \mathbf{X}_{I:J} \rangle + \hat{\underline{\mathbf{T}}}_{I:J}^{\mathrm{v*}} \langle \mathbf{X}_{I:J} \rangle \right] \mathrm{d}V_{\mathbf{X}_J} - \mathbf{b}_I = 0,$$
(19)

where $\hat{\underline{\mathbf{T}}}_{I:J}^{\mathrm{d}}$ and $\hat{\underline{\mathbf{T}}}_{I:J}^{\mathrm{v*}}$ are given in (16) and (18). The resulting formulation is termed Godunov-peridynamics.

3.2 Discussion

To examine the properties of the algorithm and to define the Riemann problem, (18) is first rewritten in the following form

$$\hat{\underline{\mathbf{T}}}_{I:J}^{\mathrm{v*}} = P_{IJ}^* \boldsymbol{\alpha}_{IJ},$$
(20)

with

$$\begin{aligned}\boldsymbol{\alpha}_{IJ} &= \mathbf{F}_I^{-T} \cdot \mathbf{K}_I^{-1} \cdot \mathbf{X}_{I:J} \det(\mathbf{F}_I)\omega_{I:J}, \\ &\quad + \mathbf{F}_J^{-T} \cdot \mathbf{K}_J^{-1} \cdot \mathbf{X}_{I:J} \det(\mathbf{F}_J)\omega_{I:J}.\end{aligned}$$
(21)

With nodal integration (further discussed in Sect. 4.1), the total driving internal force density $\mathbf{f}_I^{\mathrm{v*}}$ at point I due to pressure in (20) is expressed as

$$\mathbf{f}_I^{\mathrm{v*}} = \sum_{J \in \mathcal{N}_I} P_{IJ}^* \boldsymbol{\alpha}_{IJ} V_J,$$
(22)

where $\mathcal{N}_I$ is the set containing the point indices within the horizon of point I and V_J is the integration weight assigned to point J. The term $\boldsymbol{\alpha}_{IJ}$ in the above can be seen to control
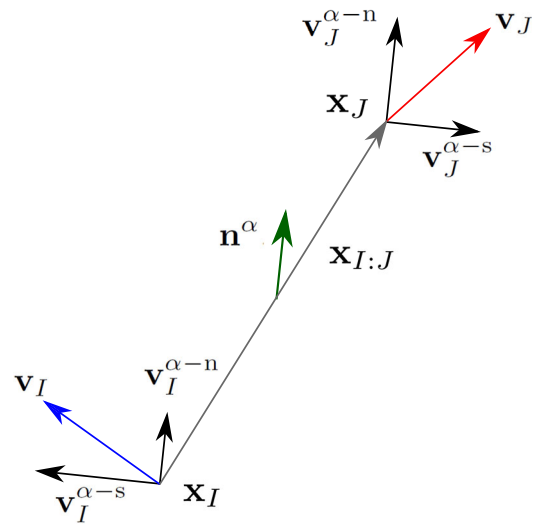

Fig. 2 Velocity projection in the deformed configuration

the contribution of the pressure to a given point I from point J.

On the other hand, a finite volume method calculates the driving force $\bar{\mathbf{f}}_I^{\mathrm{v*}}$ from the enriched pressure for a cell I from faces J of its neighboring cells as [30]

$$\bar{\mathbf{f}}_I^{\mathrm{v*}} = \sum_{J \in \mathcal{F}_I} P_{IJ}^* \bar{\boldsymbol{\alpha}}_{IJ} V_J,$$
(23)

where $\mathcal{F}_I$ is the set containing faces indices for cell I, and

$$\bar{\boldsymbol{\alpha}}_{IJ} = \frac{\boldsymbol{n}_{IJ} A_{IJ}}{V_I V_J}$$
(24)

is the equivalent coefficient for the finite volume method, with $\boldsymbol{n}_{IJ}$ the surface normal and A_{IJ} the surface area shared by cell I and J. Therefore, the coefficient $\boldsymbol{\alpha}_{IJ}$ for the proposed formulation can be interpreted as containing effective surface information between point pairs, with $\mathbf{n}^\alpha = \boldsymbol{\alpha}_{IJ}/|\boldsymbol{\alpha}_{IJ}|$ the effective normal, and will be the basis of the present Godunov implementation in Sect. 4.2.

Note that by substituting $\mathbf{X}_{I:J} = -\mathbf{X}_{I:J}$ into (21), it is obvious that

$$\boldsymbol{\alpha}_{IJ} = -\boldsymbol{\alpha}_{JI}.$$
(25)

This antisymmetric property is again shared by finite volume cells where the normal of one cell is opposite to that shared by its neighboring cells yielding $\bar{\boldsymbol{\alpha}}_{IJ} = -\bar{\boldsymbol{\alpha}}_{JI}$, which is critical to ensure conservation in the finite volume method [30]. The antisymmetric property of $\boldsymbol{\alpha}_{IJ}$ in the present formulation means that the force exchange due to pressure between points I and J is equal and opposite in the case that $V_I = V_J$.

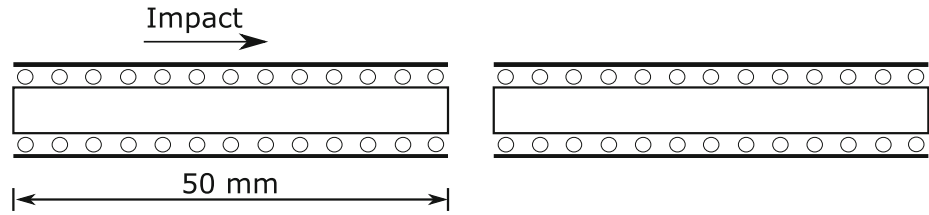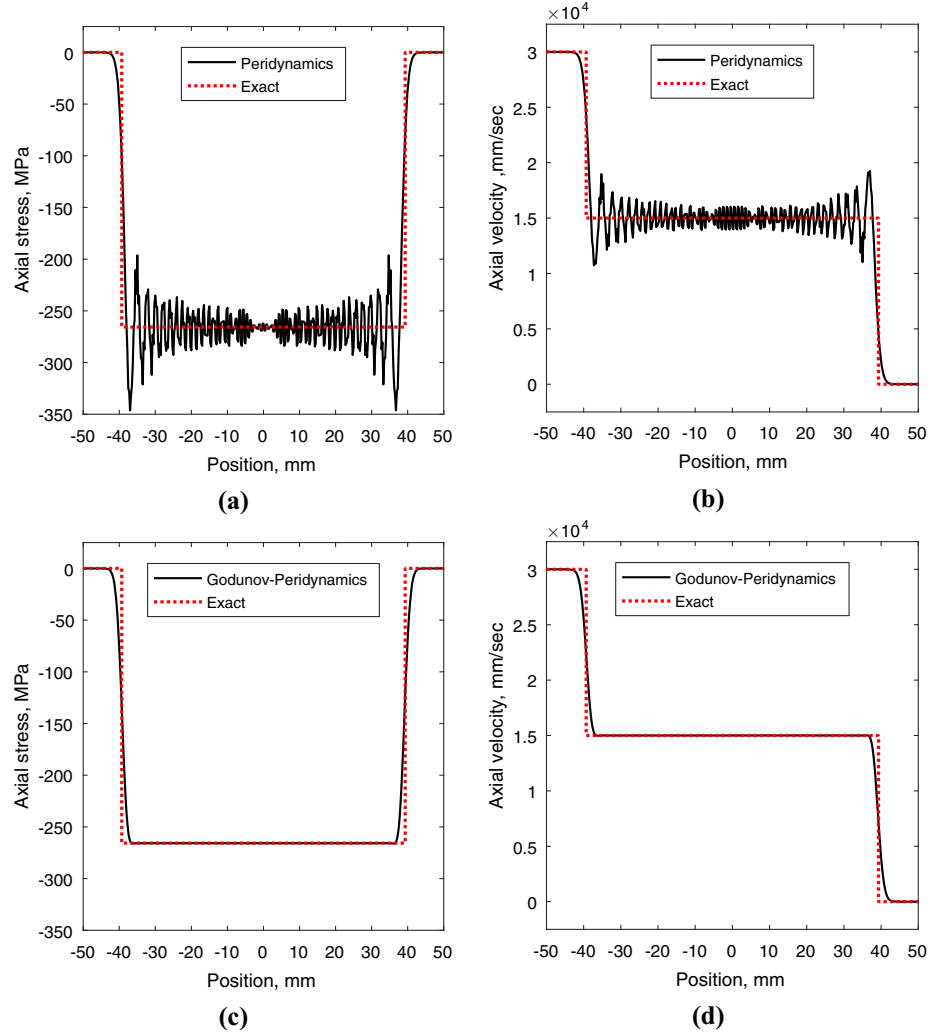**Fig. 3** Schematic of one-dimensional elastic bar impact problem

Fig. 4 One-dimensional elastic bar impact: axial stress and velocity distribution at time $t = 6\,\mu s$, **a**, **b** by peridynamics, **c**, **d** by Godunov-peridynamics

(a)

(b)

(c)

(d)

4 Numerical implementation

This section describes the numerical implementation of Godunov-peridynamics. Nodal quadrature used to numerically evaluate domain integrals is given, along with the Riemann problem solution and time integration procedures.

4.1 Nodal integration

As can be seen, **F** in (3), **K** in (4), and the second term in (19) require numerical integration. After discretization as shown in Fig. 1, the nodal integration scheme is employed [31] and
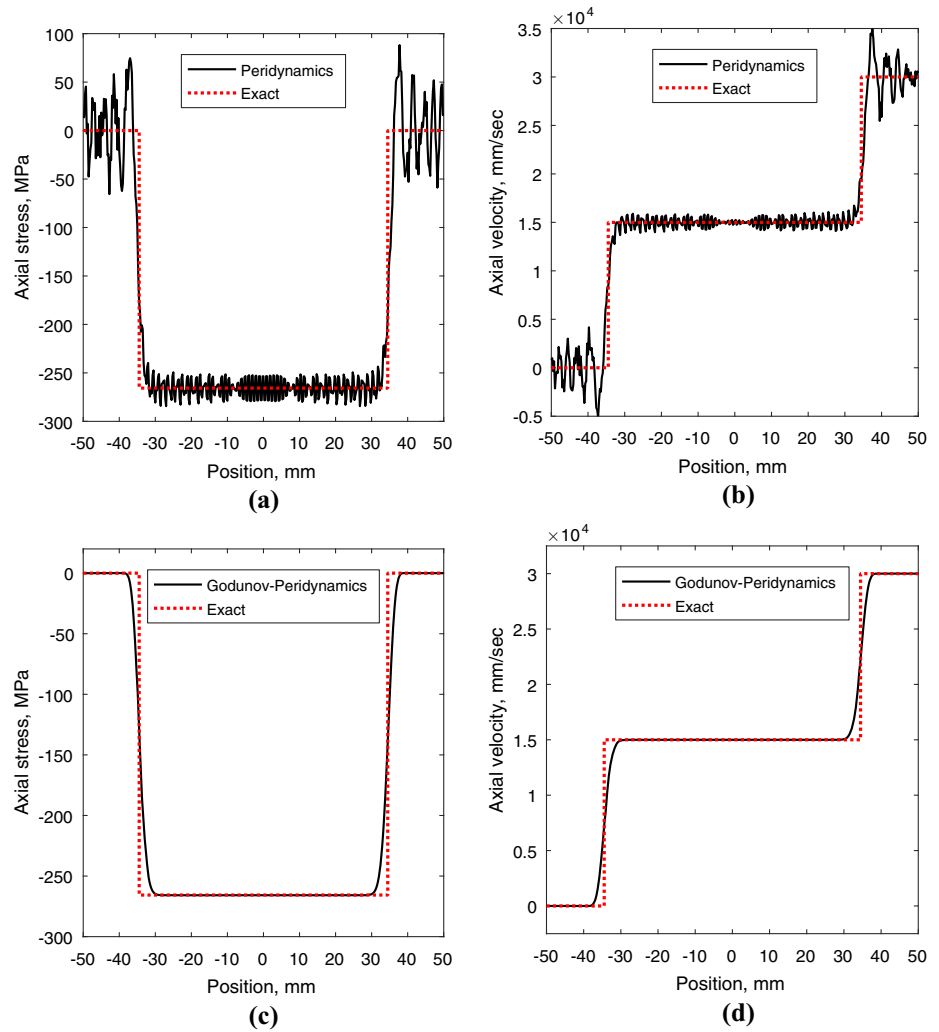
these terms are computed as

$$\mathbf{K}_I = \sum_{J \in \mathcal{N}_I} \omega_{I:J} \mathbf{X}_{I:J} \otimes \mathbf{X}_{I:J} V_J, \tag{26}$$

$$\mathbf{F}_I = \sum_{J \in \mathcal{N}_I} \omega_{I:J} \mathbf{x}_{I:J} \otimes \mathbf{X}_{I:J} V_J, \tag{27}$$

and

$$\rho_I \ddot{\mathbf{u}}_I - \sum_{J \in \mathcal{N}_I} \left[\hat{\underline{\mathbf{T}}}_{I:J}^{\mathrm{d}} \langle \mathbf{X}_{I:J} \rangle + \hat{\underline{\mathbf{T}}}_{I:J}^{\mathrm{v*}} \langle \mathbf{X}_{I:J} \rangle \right] V_J - \mathbf{b}_I = 0. \tag{28}$$

Fig. 5 Elastic bar impact: axial stress and velocity distribution at time $t = 10\,\mu s$, **a**, **b** by peridynamics, **c**, **d** by Godunov-peridynamics

While the quadrature employed is inherently low-order, influence functions such as the cubic spline (5) help to reduce inaccuracy in integration and yield more consistent solution convergence behavior [29].

4.2 Riemann solution

In (18), the term $\hat{\underline{\mathbf{T}}}_{I:J}^{v*}$ involves P_{IJ}^* which is obtained by solving the Riemann problem at the middle point between point I and J.

First, a piecewise distribution in pressure and velocity is assumed to eliminate Gibbs instability: Between point I and the middle point, and point J and the middle point, the pressure and velocity are assumed to be constant. The Riemann problem is then solved along the effective normal direction between the two nodes in the deformed configuration $\mathbf{n}^\alpha = \boldsymbol{\alpha}_{IJ}/|\boldsymbol{\alpha}_{IJ}|$, as shown in Fig. 2, with the normal velocity calculated as

$$v_I^{\alpha-n} = \mathbf{v}_I \cdot \mathbf{n}^\alpha. \tag{29}$$

The Riemann problem then consists of a left state $\{P_I, v_I^{\alpha-n}, \rho_I\}$ and right state $\{P_J, v_J^{\alpha-n}, \rho_J\}$, with the solution $\{P_{IJ}^*, v_{IJ}^{\alpha-n*}\}$. In "Appendix", the Dukowicz Riemann solver [32] employed in this work is given for convenience.

4.3 Time integration procedures

For clarity in describing the time integration procedure, Eq. (28) is rewritten in the following form,
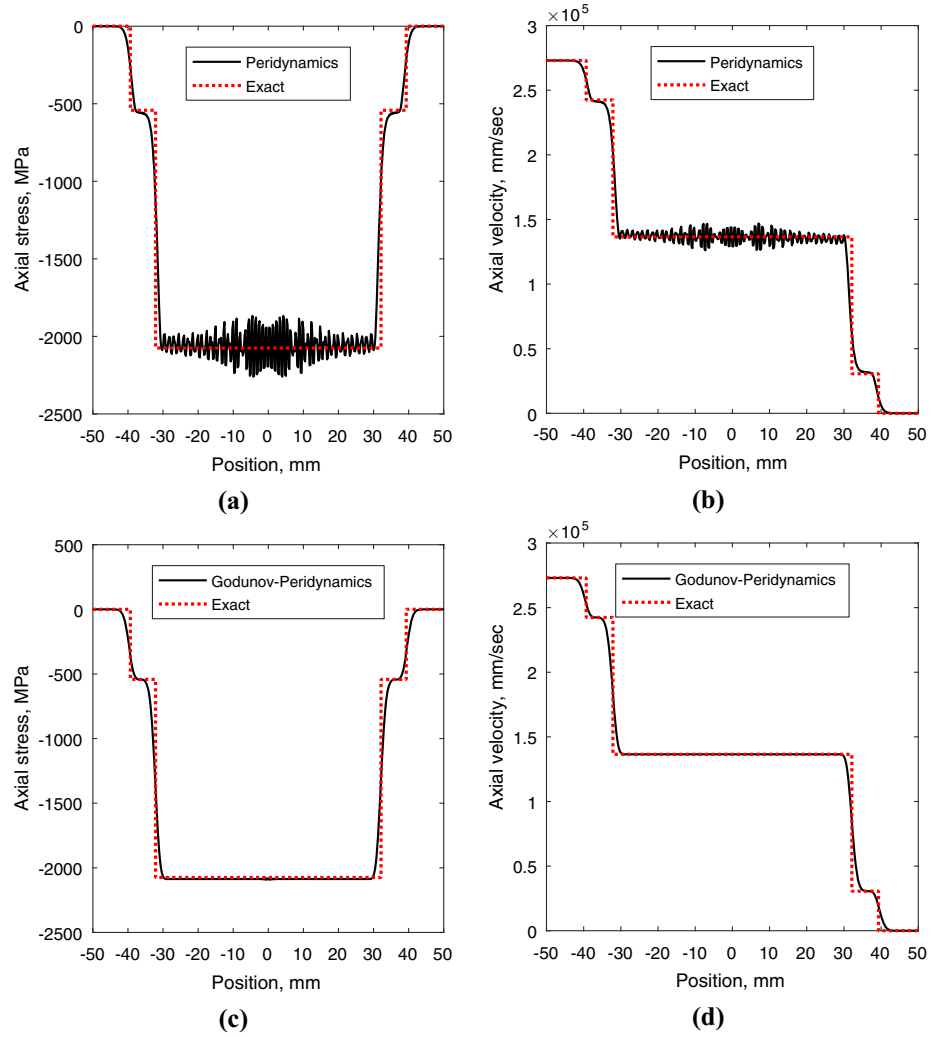
$$\rho_I \ddot{\mathbf{u}}_I = \mathbf{f}_I^d + \mathbf{f}_I^{v*} + \mathbf{b}_I, \tag{30}$$

with

$$\mathbf{f}_I^d = \sum_{J \in \mathcal{N}_I} \left[\hat{\underline{\mathbf{T}}}_{I:J}^d \langle \mathbf{X}_{I:J} \rangle \right] V_J, \tag{31}$$

$$\mathbf{f}_I^{v*} = \sum_{J \in \mathcal{N}_I} \left[\hat{\underline{\mathbf{T}}}_{I:J}^{v*} \langle \mathbf{X}_{I:J} \rangle \right] V_J. \tag{32}$$

Fig. 6 Elasto-plastic bar impact: axial stress and velocity distribution at time $t = 6\,\mu s$, **a**, **b** by peridynamics, **c**, **d** by Godunov-peridynamics

(a)

(b)

(c)

(d)

The Newmark-beta method is employed to perform temporal discretization of Eq. (30) with $\beta = 0$ and $\gamma = \frac{1}{2}$ resulting in the explicit central difference scheme. In what follows, the superscript (n) denotes a variable at the nth time step. The central difference time integration procedures for a point I in a predictor–corrector implementation are given as:

(1) Initialization:

  (a) Form initial $\mathbf{b}_I^{(0)}$.

  (b) Calculate initial acceleration $\mathbf{a}_I^{(0)}$ by
$$\rho_I \mathbf{a}_I^{(0)} = \mathbf{b}_I^{(0)}.$$

(2) At the $(n + 1)$th time step:

  (a) Predictor phase: calculate displacement predictor $\tilde{\mathbf{u}}_I$ and velocity predictor $\tilde{\mathbf{v}}_I$
$$\tilde{\mathbf{u}}_I^{(n+1)} = \mathbf{u}_I^{(n)} + \Delta t \mathbf{v}_I^{(n)} + \frac{\Delta t^2}{2} \mathbf{a}_I^{(n)},$$
$$\tilde{\mathbf{v}}_I^{(n+1)} = \mathbf{v}_I^{(n)} + \frac{\Delta t}{2} \mathbf{a}_I^{(n)}.$$

  (b) Calculate $\boldsymbol{\tau}_I^{d(n+1)}$ and $P_I^{(n+1)}$.

  (c) Calculate Riemann solution for point I's pairs.

  (d) Calculate $\mathbf{f}_I^{d(n+1)}$ and $\mathbf{f}_I^{v*(n+1)}$ according to Eq. (31) and (32), respectively, and also compute $\mathbf{b}_I^{(n+1)}$.

  (e) Solve $\rho_I \mathbf{a}_I^{(n+1)} = \mathbf{f}_I^{d(n+1)} + \mathbf{f}_I^{v*(n+1)} + \mathbf{b}_I^{(n+1)}$ for acceleration $\mathbf{a}_I^{(n+1)}$.

  (f) Corrector phase:

$$\mathbf{v}_I^{(n+1)} = \mathbf{v}_I^{(n)} + \frac{\Delta t}{2}(\mathbf{a}_I^{(n)} + \mathbf{a}_I^{(n+1)}),$$
$$\mathbf{u}_I^{(n+1)} = \tilde{\mathbf{u}}_I^{(n+1)}.$$

(3) If time t is less than the total simulation time t_{final}, set $n \to n + 1$ and go to (a) in step (2).

Compared with the standard non-ordinary state-based peridynamics formulation (without shock enrichment), all of the procedures here in Godunov-peridynamics are the same except that the volumetric force portion is evaluated by Eq. (32) with Riemann solution enriched pressure P_{IJ}^*.
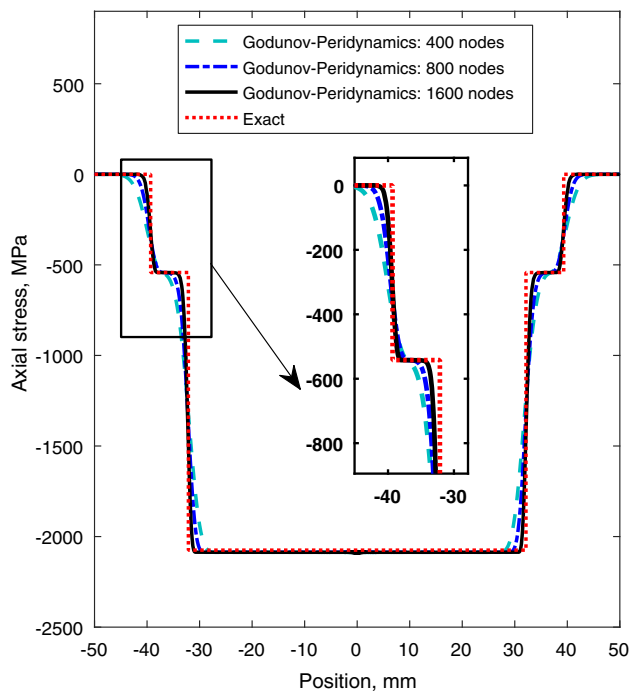
Fig. 7 One-dimensional elasto-plastic bar impact: axial stress distribution with different discretizations at time $t = 6\,\mu s$

5 Numerical examples

In all the numerical examples, uniform point distributions are used; the radius of the horizon is set to be 1.65 times the spacing, and the cubic spline influence function (5) is employed. All examples are impact problems. The impact is not explicitly modeled as a contact condition; instead, it is achieved by modeling the impact and target objects as one body with different initial velocities, where the shock physics moments before the bars physically separate are observed. The terms "peridynamics" and "Godunov-peridynamics" are used to denote the results obtained by the non-ordinary state-based peridynamics and the proposed Godunov-peridynamics formulations.

The exact solutions used in all of the following examples are based on the classical continuum theory which is a local theory; nevertheless, they still serve as reference solutions for peridynamics since the non-local formulation converges to the classical solution provided the horizon approaches zero [33,34]. As such, in the refinement study in Sect. 5.2 reduces the nodal horizon and nodal spacing simultaneously at a fixed ratio, such that the numerical formulation will converge to the classical local solution that it is tested against [34].

5.1 Elastic bar impact

A one-dimensional elastic bar impact problem shown in Fig. 3 is solved as the first example. The bars are made of 6061
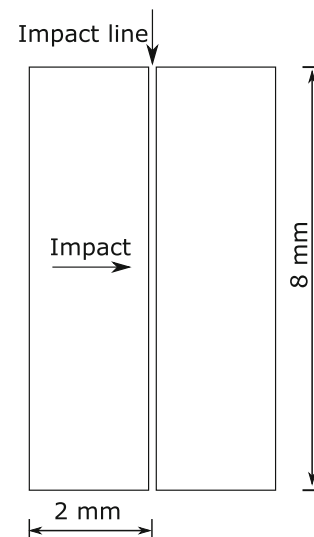

**Fig. 8** Schematic of high-velocity plate impact problem

T-6 aluminum, which is described by a J_2 perfect plasticity material model. The material properties are given as Young's modulus $E = 77.11\,\text{GPa}$, Poisson's ratio $\nu = 0.334$, density $\rho = 2703\,\text{kg/m}^3$, and yield strength $Y_0 = 270\,\text{MPa}$. The deformation is only allowed along the axial direction and the lateral direction is constrained by rollers (see Fig. 3). The initial velocity of the impact bar is $3.00 \times 10^4\,\text{mm/s}$, and that of the target bar is $0.00\,\text{mm/s}$, which results in elastic waves in the bars due to the relatively low impact velocity. Both bars have a length of 50 mm and are discretized with 800 points in the axial direction. The analytical solution of this problem can be derived by making use of the Rankine–Hugoniot jump conditions (see [35]). We consider the solution at two different moments: at time $6\,\mu s$ (before free end reflection) and time $10\,\mu s$ (after free end reflection).

The numerical solutions by peridynamics and Godunov-peridynamics at time $6\,\mu s$ are given in Fig. 4. After free end reflection, at time $10\,\mu s$, the resulting axial stress and velocity magnitudes remain the same as at time $6\,\mu s$. The associated numerical results for both formulations are shown in Fig. 5. As can be seen, the results by peridynamics in both cases show severe oscillations in stress and velocity.

5.2 Elasto-plastic bar impact

This problem is similar to the example in Sect. 5.1 but with a higher impact velocity $2.73 \times 10^5\,\text{mm/s}$. The geometry size, material properties, boundary conditions, and discretization of the bars are the same as in the previous problem. The higher impact velocity of $2.73 \times 10^5\,\text{mm/s}$ is chosen such that the yield strength is reached, and as a result, an elastic shock wave is formed, followed by a plastic shock wave. Here the solution at time $6\,\mu s$ is examined. The numerical solu-

Fig. 9 High-velocity plate impact pressure contours: left two (left to right), peridynamics and Godunov-peridynamics results at time $t = 0.075\,\mu s$, and right two (left to right), peridynamics and Godunov-peridynamics results at time $t = 0.25\,\mu s$
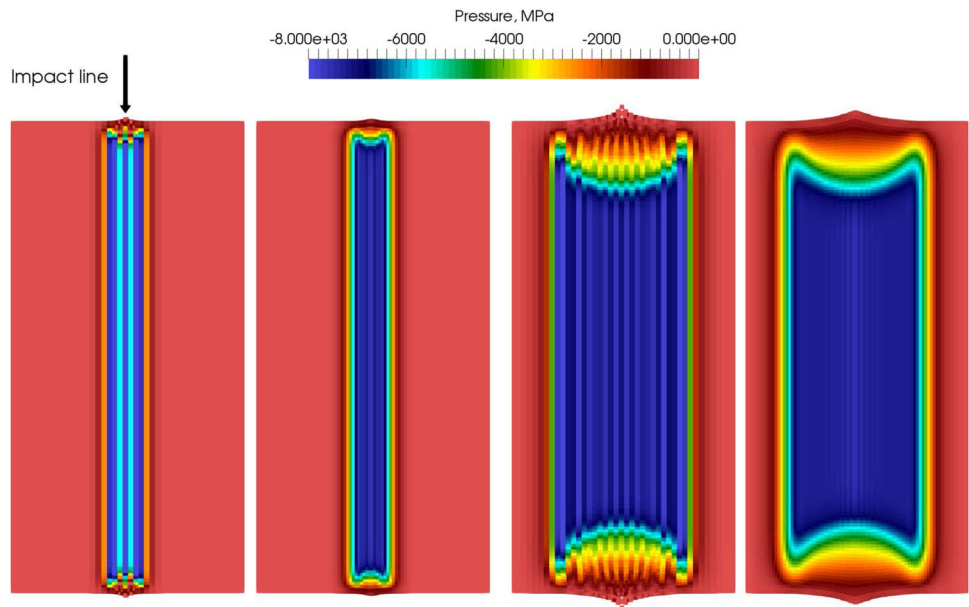
tions by peridynamics and Godunov-peridynamics are given in Fig. 6 and compared with the exact solution [35]. Both formulations give the correct shock speeds and jump magnitudes if the averaged magnitudes are used for the oscillatory peridynamics results; however, the peridynamics solutions show severe oscillations, while the Godunov-peridynamics formulation offers a non-oscillatory solution. A set of discretizations, 400 points, 800 points, and 1600 points in the axial direction are used to check the solution convergence, and the result is given in Fig. 7. Here the ratio of horizon to nodal spacing is fixed at 1.65, such that the numerical solution should converge to the local solution [34]. In the enlarged subfigure, one can observe that the numerical solution by Godunov-peridynamics converges.

5.3 High-velocity plate impact

Here, a two-dimensional plane-strain high-velocity plate impact problem is modeled. A flyer plate with a velocity of 1.00×10^{6} mm/s impacts another plate that is initially static. All in-plane edges are unconstrained resulting in multi-dimensional wave propagation. After the compression shock wave reaches the free surface, a rarefaction wave is formed and propagates inside from the outer edges. Each plate is 8 mm wide by 2 mm thick (see Fig. 8) and is discretized as 161 points by 41 points, in each direction, respectively. The impact occurs along the longer 8 mm edge. The material is again 6061 T-6 aluminum, modeled with the same material properties and constitutive model as in the previous problems. The pressure contours at time $t = 0.075\,\mu s$ and $t = 0.25\,\mu s$ are provided in Fig. 9. Consistent with the above discussion, a compression shock wave is first generated and then propagates along the impact direction, and a rarefaction

wave forms from the lateral edges, which relieves the pressure in the initially compression-loaded zone. This pressure relief phenomenon in the boundary normal direction is similar to the case shown in Fig. 5 of the one-dimensional elastic bar impact problem in Sect. 5.1.

Peak pressure behind the shock wave was experimentally measured by Marsh [36] as 8.00 GPa. Here, the result by peridynamics is 9.01 GPa with 12.63% error, whereas Godunov-peridynamics gives a more accurate peak pressure of 7.61 GPa with 4.87% error. On the other hand, the two pressure contours by Godunov-peridynamics at two these time instances are both essentially free of oscillation while the solutions by peridynamics are highly oscillatory. This example also shows the ability to accurately solve problems involving multi-dimensional shockwave propagation by Godunov-peridynamics.

6 Conclusion

In this paper, a shock modeling formulation termed Godunov-peridynamics is proposed that incorporates shock physics by employing the Godunov scheme into non-ordinary state-based peridynamics. The essential shock physics of entropy and jump conditions are considered by introducing the Riemann problem solution into the volumetric portion of the force state. The Riemann problem is defined at the middle point of each point pair via effective surface information $\boldsymbol{\alpha}$ in the deformed configuration. The antisymmetric property of $\boldsymbol{\alpha}$ ensures a volumetric force state conservation in uniform discretizations where equal integration weights are employed. The resulting formulation does not introduce any tunable

parameters and controls the oscillations otherwise induced by shocks.

This work also provides a general technique to bridge the Godunov scheme and other numerical methods when effective surface information $\boldsymbol{\alpha}$ in (22) can be obtained.

Several benchmark problems involving one-dimensional and two-dimensional shocks are examined, where non-oscillatory solutions with high accuracy are obtained under the present formulation. Future effort will be devoted to applying this formulation to shock-induced fragmentation by incorporating bond breakage and material damage.

Compliance with ethical standards

Conflict of interest On behalf of all authors, the corresponding author states that there is no conflict of interest.

Appendix

Here, a brief overview of the Dukowicz Riemann solver [32] employed in this work is given. Consider a left state $\{P_L, v_L, \rho_L\}$ and right state $\{P_R, v_R, \rho_R\}$, with the solution $\{P^*, v^*\}$. In this solver, the velocity v^* is first computed by solving the following semi-quadratic equation,

$$
\rho_L B_L |v^* - v^*_{min}|(v^* - v^*_{min}) + \rho_R B_R |v^* - v^*_{max}|(v^* - v^*_{max}) + P^*_L - P^*_R, \tag{33}
$$

where

$$
\begin{aligned}
v^*_{min} &= v_L - 0.5C_L/B_L, \\
v^*_{max} &= v_R - 0.5C_R/B_R; \\
P^*_L &= P_L - 0.25\rho_L(C_L)^2/B_L, \\
P^*_R &= P_R - 0.25\rho_R(C_R)^2/B_R.
\end{aligned} \tag{34}
$$

Here, C is the speed of sound and B is a parameter that is directly related to the shock density ratio in the limit of strong shocks (for more details, refer to [32]). Equation (33) becomes a quadratic equation after assuming a sign for $(v^* - v^*_{min})$ and $(v^* - v^*_{max})$ yielding four cases in total. One of the two roots of each quadratic equation can be abandoned in advance, and the other root left is the unique solution for each case. Once the velocity v* is solved, the pressure solution P^* can be readily calculated by the following equation,

$$
P^* = 0.5(P^*_L + P^*_R) + 0.5\rho_L B_L |v^* - v^*_{min}|(v^* - v^*_{max}) - 0.5\rho_R B_R |v^* - v^*_{max}|(v^* - v^*_{min}). \tag{35}
$$

As can be seen, this Riemann solver is non-iterative.

In the end, the obtained P^* is used as P^*_{IJ} in (18) to compute the Riemann solution enriched volumetric force state.

References

1. Silling SA (2000) Reformulation of elasticity theory for discontinuities and long-range forces. J Mech Phys Solids 48(1):175–209
2. Silling SA, Epton M, Weckner O, Xu J, Askari E (2007) Peridynamic states and constitutive modeling. J Elast 88(2):151–184
3. Ha YD, Bobaru F (2010) Studies of dynamic crack propagation and crack branching with peridynamics. Int J Fract 162(1–2):229–244
4. Bobaru F, Zhang G (2015) Why do cracks branch? A peridynamic investigation of dynamic brittle fracture. Int J Fract 196(1–2):59–98
5. Bobaru F, Ha YD, Hu W (2012) Damage progression from impact in layered glass modeled with peridynamics. Cent Eur J Eng 2(4):551–561
6. Gerstle W, Sau N, Silling S (2007) Peridynamic modeling of concrete structures. Nucl Eng Des 237(12–13):1250–1258
7. Tupek MR, Rimoli JJ, Radovitzky R (2013) An approach for incorporating classical continuum damage models in state-based peridynamics. Comput Methods Appl Mech Eng 263:20–26
8. Foster JT, Silling SA, Chen WW (2010) Viscoplasticity using peridynamics. Int J Numer Methods Eng 81(10):1242–1258
9. Warren TL, Silling SA, Askari A, Weckner O, Epton MA, Xu J (2009) A non-ordinary state-based peridynamic method to model solid material deformation and fracture. Int J Solids Struct 46(5):1186–1195
10. Ren B, Fan H, Bergel GL, Regueiro RA, Lai X, Li S (2014) A peridynamics-SPH coupling approach to simulate soil fragmentation induced by shock waves. Comput Mech 55(2):287–302
11. Lai X, Liu L, Li S, Zeleke M, Liu Q, Wang Z (2018) A non-ordinary state-based peridynamics modeling of fractures in quasi-brittle materials. Int J Impact Eng 111:130–146
12. Silling SA, Parks ML, Kamm JR, Weckner O, Rassaian M (2017) Modeling shockwaves and impact phenomena with Eulerian peridynamics. Int J Impact Eng 107:47–57
13. Godunov SK (1969) A finite difference method for numerical computation of discontinuous solutions of the equations of fluid dynamics. Sb Math 47:271–306
14. Cockburn B, Shu CW (1998) The Runge–Kutta discontinuous Galerkin method for conservation laws V. J Comput Phys 141(2):199–224
15. Inutsuka SI (2002) Reformulation of smoothed particle hydrodynamics with Riemann solver. J Comput Phys 179(1):238–267
16. Löhner R, Sacco C, Oñate E, Idelsohn SR (2002) A finite point method for compressible flow. Int J Numer Methods Eng 53(8):1765–1779
17. Dukowicz JK, Cline MC, Addessio FL (1989) A general topology Godunov method. J Comput Phys 82(1):29–63
18. Hietel D, Steiner K, Struckmeier J (2000) A finite volume particle method for compressible flows. Math Models Methods Appl Sci 10:1363–1382
19. Chiu EK, Wang Q, Jameson A (2011) A conservative meshless scheme: general order formulation and application to Euler equations. In: AIAA 2011-651 49th Aerospace Sciences Meeting
20. Luo H, Baum JD, Loehner R (1994) Edge-based finite element scheme for the Euler equations. AIAA J 32(6):1183–1190
21. Praveen C (2004) A positive meshless method for hyperbolic equations. Technical Report, Department of Aerospace Engineering, Indian Institute of Science

22. Ma ZH, Wang H, Qian L (2014) A meshless method for compressible flows with the HLLC Riemann solver 44(0):1–24 arXiv preprint arXiv:1402.2690

23. van Leer B (1979) Towards the ultimate conservative difference scheme. V. A second-order sequel to Godunov's method. J Comput Phys 32(1):101–136

24. Liu WK, Jun S, Zhang YF (1995) Reproducing kernel particle methods. Int J Numer Methods Fluids 20(8–9):1081–1106

25. Chen JS, Pan C, Wu CT, Liu WK (1996) Reproducing kernel particle methods for large deformation analysis of non-linear structures. Comput Methods Appl Mech Eng 139(1–4):195–227

26. Chen JS, Wu CT, Yoon S, You Y (2001) A stabilized conforming nodal integration for Galerkin mesh-free methods. Int J Numer Methods Eng 50(2):435–466

27. Roth MJ, Chen JS, Danielson KT, Slawson TR (2016) Hydrodynamic meshfree method for high-Rate solid dynamics using a Rankine–Hugoniot enhancement in a Riemann-SCNI framework. Int J Numer Methods Eng 108:1525–1549

28. Roth MJ, Chen JS, Slawson TR, Danielson KT (2016) Stable and flux-conserved meshfree formulation to model shocks. Comput Mech 57(5):773–792

29. Seleson P, Littlewood DJ (2016) Convergence studies in meshfree peridynamic simulations. Comput Math Appl 71(11):2432–2448

30. LeVeque RJ (2002) Finite volume methods for hyperbolic problems, vol 31. Cambridge University Press, Cambridge

31. Silling SA, Askari E (2005) A meshfree method based on the peridynamic model of solid mechanics. Comput Struct 83(17–18):1526–1535

32. Dukowicz JK (1985) A general, non-iterative Riemann solver for Godunov's method. J Comput Phys 61(1):119–137

33. Silling SA, Lehoucq RB (2008) Convergence of peridynamics to classical elasticity theory. J Elast 93(1):13

34. Bobaru F, Yang M, Alves LF, Silling SA, Askari E, Xu J (2009) Convergence, adaptive refinement, and scaling in 1d peridynamics. Int J Numer Methods Eng 77(6):852–877

35. Davison L (2008) Fundamentals of shock wave propagation in solids. Springer, Berlin

36. Marsh SA (1980) LASL shock Hugoniot data. Technical report, University of California Press, Berkley